Molecular Cell
Article

The Mechanism of Prion Inhibition by HET-S

Jason Greenwald,[1] Carolin Buhtz,[1] Christiane Ritter,[2] Witek Kwiatkowski,[3] Senyon Choe,[3] Marie-Lise Maddelein,[4] Frederique Ness,[4] Sandra Cescau,[4] Alice Soragni,[1] Dominik Leitz,[1] Sven J. Saupe,[4] and Roland Riek[1,3,*]
[1]Laboratory of Physical Chemistry, ETH Zürich, Wolfgang-Pauli-Strasse 10, 8093 Zürich, Switzerland
[2]Helmholtz Center for Infection Research, Inhoffenstraße 7, 38124 Braunschweig, Germany
[3]Structural Biology Laboratory, The Salk Institute for Biological Studies, 10010 North Torrey Pines Road, La Jolla, CA 92037, USA
[4]Laboratoire de Génétique Moléculaire des Champignons, Institut de Biochimie et Génétique Cellulaires, UMR-5095 CNRS/Université de Bordeaux 2, 1 rue Camille St Saëns, 33077 Bordeaux, France
*Correspondence: roland.riek@phys.chem.ethz.ch
DOI 10.1016/j.molcel.2010.05.019

SUMMARY

HET-S (97% identical to HET-s) has an N-terminal globular domain that exerts a prion-inhibitory effect in *cis* on its own prion-forming domain (PFD) and in *trans* on HET-s prion propagation. We show that HET-S fails to form fibrils in vitro and that it inhibits HET-s PFD fibrillization in *trans*. In vivo analyses indicate that β-structuring of the HET-S PFD is required for HET-S activity. The crystal structures of the globular domains of HET-s and HET-S are highly similar, comprising a helical fold, while NMR-based characterizations revealed no differences in the conformations of the PFDs. We conclude that prion inhibition is not encoded by structure but rather in stability and oligomerization properties: when HET-S forms a prion seed or is incorporated into a HET-s fibril via its PFD, the β-structuring in this domain induces a change in its globular domain, generating a molecular species that is incompetent for fibril growth.

INTRODUCTION

Prions are self-propagating, usually amyloid-like protein aggregates (Aguzzi et al., 2008). In mammals, prions cause fatal neurodegenerative disease, while in fungi they are detected as protein-based genetic elements (Wickner et al., 2008). The fungal prion proteins have a modular organization comprising a so-called prion-forming domain (PFD) that is natively unfolded in the soluble form and that is appended to a globular domain. While the PFD of these proteins is both necessary and sufficient for prion propagation, the in vivo prion-forming abilities and aggregate morphology of a given protein can be strongly affected by mutations or polymorphism in the appended globular domain (Balguerie et al., 2003, 2004; Fernandez-Bellot et al., 2000; Liu et al., 2002; Maddelein and Wickner, 1999; Masison and Wickner, 1995). This is apparently true for amyloidogenic proteins in general, as it has also been shown that amyloid toxicity of polyQ aggregates is strongly dependent on flanking domains (Dehay and Bertolotti, 2006; Duennwald et al., 2006). While considerable efforts have been devoted to the structural and functional characterization of the PFDs of fungal prions, the mechanistic basis of this *cis*-regulatory effect has been only scarcely studied despite its importance in the prion propagation mechanism. The *het-s*/*het-S* fungal prion may be the most blatant example of such a *cis*-acting prion-inhibitory domain (Balguerie et al., 2003, 2004). HET-s and HET-S are natural polymorphic variants of the same protein that share a functional C-terminal PFD. Yet, in contrast to HET-s, full-length HET-S totally lacks prion-forming ability in vivo.

In the filamentous fungus *Podospora anserina*, the prion state of the HET-s protein is involved in a programmed cell death (PCD) reaction termed heterokaryon incompatibility. Filamentous fungi have several incompatibility loci that regulate the fusion of mycelium between genetically distinct individuals (Glass et al., 2000; Saupe, 2000). The *het-s* locus has two antagonistic alleles: *het-s* and *het-S*. Their encoded proteins, HET-s and HET-S, give rise to the compatibility phenotypes [Het-s] and [Het-S]. Although they differ by only 13 out of 289 residues (Turcq et al., 1991), only HET-s undergoes a transition to an infectious prion state that is correlated in vivo with the conversion from the [Het-s*] to the [Het-s] phenotype (Coustou et al., 1997). When a [Het-s] strain fuses with a [Het-S] strain, the fusion cell dies, whereas the fusion of [Het-s*] with [Het-S] leads to a viable mixed cell (heterokaryon). Colonies with the [Het-s*] phenotype convert spontaneously to [Het-s] at a very low frequency, but contact between [Het-s] and [Het-s*] strains leads to infection of the latter and conversion of its phenotype to [Het-s]. Importantly, in vivo interactions between [Het-s] and [Het-S] strains can also lead to elimination of the [Het-s] prion state (Beisson-Schecroun, 1962; Dalstra et al., 2003; Rizet, 1952). This occurs, for instance, in a [Het-s] × [Het-S] sexual cross in which [Het-S] leads to complete curing of the [Het-s] prion in the meiotic progeny (daughter cells with the *het-s* allele are [Het-s*]). Using microsurgical approaches, it was also shown that [Het-S] strongly inhibits [Het-s] propagation in vegetative hyphae (Beisson-Schecroun, 1962). Therefore, [Het-S] not only triggers cell death upon interaction with [Het-s] but also exerts an inhibitory effect on its propagation.

HET-s is a two-domain protein. It comprises a C-terminal PFD (residues 218–289) that is both necessary and sufficient for amyloid formation and prion propagation and an N-terminal globular domain (residues 1 to ~227) that specifies the incompatibility type ([Het-s] or [Het-S]) (Balguerie et al., 2003). A chimeric protein construct with the HET-S globular domain appended to the HET-s PFD results in a protein of the [Het-S]

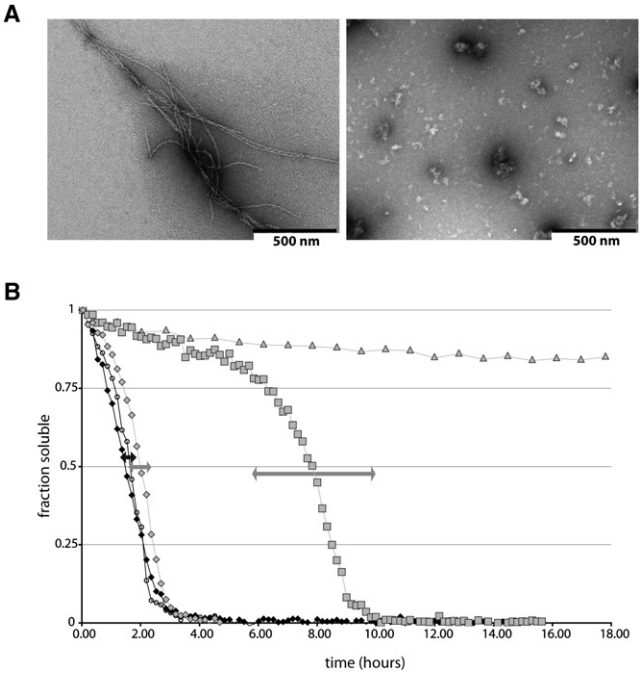

Figure 1. HET-S Does Not Form Fibrils and Can Inhibit Aggregation of HET-s PFD

(A) Electron micrographs of negatively stained aggregates of HET-s (left) and HET-S (right), both at the same magnification (scale bar in the lower right of image is 500 nm). Proteins at 15 μM were incubated 24 hr at 37°C with light agitation in 100 mM Tris-HCl (pH 8), 150 mM NaCl.

(B) Coaggregation kinetics of HET-s PFD in the presence of HET-S. The ^{15}N-filtered 1D NMR signal of the ^{15}N-labeled PFD was integrated between 6.5 and 9.0 ppm for each time point, the data normalized to the first time point, and represented as the fraction soluble. All measurements included 52 μM PFD and the plot symbols are as follows: open circles, control PFD alone; gray diamonds, 75 nM HET-S; gray squares, 750 nM HET-S; gray triangles, 7.5 μM HET-S; black diamonds, 750 nM HET-S[E86K]. The arrows represent the 95% confidence intervals for the 50% aggregation time for the measurements of 0, 75, and 750 nM HET-S (three or four measurements each with the closest to the average shown in plot). The 7.5 μM HET-S sample retained more than 70% of the PFD in solution after 65 hr, and complete aggregation occurred sometime between 65 and 110 hr.

type, and conversely a chimera associating the HET-s globular domain to the HET-S PFD displays the [Het-s] specificity. In other words, HET-S has a functional PFD, but the HET-S globular domain exerts a prion-inhibitory effect (in *cis*) on its own C-terminal PFD. A detailed analysis of the amino acid differences between HET-s and HET-S revealed that a single amino acid substitution in HET-S (H33P) converted its specificity to [Het-s] in vivo, whereas the conversion of [Het-s] to [Het-S] requires minimally two amino acid substitutions (D23A/P33H) (Deleu et al., 1993).

The molecular mechanism of HET-s-mediated heterokaryon incompatibility is not known, nor has the toxic entity that leads to cell death been identified. The reaction that occurs when incompatible strains fuse is a form of PCD that is spatially restricted to the fusion cell or one or two cells to each side. In all fungal incompatibility systems except *het-s*, one of the *het* genes involved encodes for a protein with a HET domain (no relation to the HET-s protein). It has been shown that overexpression of the HET domain alone is sufficient to induce PCD, and that it depends on the presence of two other genes (Paoletti and Clave, 2007). In contrast, no other genes have been found that are essential for *het-s*-mediated PCD, so it is possible that HET-S and HET-s form a toxic species that directly initiates PCD. Deletions in the globular domain of HET-S not only alleviate the prion-inhibitory effect of the domain but also abolish HET-S activity in incompatibility. Thus, the HET-S globular domain (but not the HET-s globular domain) is essential for PCD (Balguerie et al., 2004).

The recently reported structures of the C-terminal PFD of HET-s in its fibril form have shed light on the mechanism of prion formation and propagation (Wasmer et al., 2008; Wasmer et al., 2009). These reports revealed that the PFD aggregates into a highly ordered β-solenoid fold. However, the question remains as to how the N-terminal domain of HET-S can exert a prion-inhibitory effect on the PFD both in *cis* and in *trans*. To probe this question, we studied the functional properties of the HET-S protein in vitro and in vivo and solved the structure of the HET-s and HET-S N-terminal domains by X-ray crystallography.

RESULTS

HET-s, but Not HET-S, Forms Well-Ordered Fibrils In Vitro

We expressed and purified a soluble full-length HET-S protein (see the Experimental Procedures) allowing the comparison of the in vitro fibrillization of HET-s and HET-S. Both proteins tend to aggregate in vitro, and this can be partially suppressed by storage at 4°C. However, as revealed by negatively stained electron micrographs (Figure 1A), the aggregation of HET-s leads to long (>1 μm), well-ordered, single fibrils, while HET-S aggregates are amorphous and range in size from 10 to 100 nm. The HET-s fibril growth can be seeded by fibrils of the isolated PFD, greatly shortening the nucleation time, while the addition of PFD seeds did not lead to HET-S fibrils (data not shown). The finding that HET-S does not readily form fibrils in vitro explains the fact that [Het-S] strains do not have a prion-associated phenotype and directly illustrates the *cis*-acting prion inhibition of the HET-S globular domain.

HET-S Can Inhibit the Aggregation of the HET-s PFD In *trans*

Since the above experiments suggest that the prion inhibition mechanism of HET-S in *cis* can be recapitulated in vitro, we wondered whether the same was true for the *trans*-acting prion-inhibitory effect of HET-S on [Het-s] propagation. Thus, we looked at the ability of HET-S to inhibit fibril formation in *trans*. The aggregation kinetics of the PFD from HET-s were monitored by solution NMR in the presence of unlabeled HET-S. In this experiment, only the monomeric PFD is detected, so that the decay of the signal is proportional to the amount of PFD that has been recruited into large, presumably fibrillar aggregates. In order to minimize the stochastic nature of self-seeded aggregation kinetics, the experiments were started with the addition of 30 nM PFD fibril seeds (see the Experimental Procedures). We

Table 1. Crystallographic Data and Refinement Statistics

Model (PDB ID)	HET-s(1–227) (2wvn)	HET-S(1–227) (2wvo)	HET-s[D23A,P33H](13–221) (2wvq)
Space group	p432	p3221	p21
Unit cell dimensions			
a, b, c (Å)	122.6	95.1, 95.1, 170.4	49.3, 83.2, 67.4
α, β, γ (°)	90	90, 90, 120	90.0, 104.5, 90.0
Resolution range (outer shell) (Å)	40–2.62 (2.77–2.62)	40–2.3 (2.44–2.3)	65–2.0 (2.12–2)
Number of unique reflections	10,044	40,556	34,078
Redundancy	10.1 (10.2)	7.0 (6.2)	3.2 (3.0)
I/sigma	24.1 (3.9)	23.8 (3.6)	10.5 (3.7)
R_{meas}[a]	0.060 (0.463)	0.048 (0.569)	0.088 (0.459)
Completeness %	99.7 (99.0)	99.3 (99.1)	95.2 (93.3)
Number of protein monomers in A.U.	1	2	2
Number of nonhydrogen atoms in refinement			
Protein	1696	3533	3363
DTT	–	–	16
Chloride ion	–	4	–
Water	–	135	198
R factor/free R factor[b]	0.216/0.270	0.225/0.257	0.225/0.269
Rmsd bond lengths/angles[c]	0.018/1.843	0.010/1.411	0.016/1.739

[a] $R_{meas} = \sum_h (n_h/(n_h-1))^{1/2} \sum_i |I_i(h) - < I(h) > | / \sum_h \sum_i I_i(h)$, where $I_i(h)$ and $< I(h) >$ are the i^{th} and mean intensity, and n_h is the multiplicity over all symmetry-equivalent reflections h (Diederichs and Karplus, 1997).

[b] $R = \sum ||F_C| - |F_O|| / \sum |F_O|$, where $|F_C|$is the calculated structure factor amplitude of the model, and $|F_O|$is the observed structure factor amplitude; the free R factor was calculated against a random 5% test set of reflections that was not used during refinement. The same test set was used for all seven data sets.

[c] Rmsd, root-mean-square deviation from the parameter set for ideal stereochemistry (Engh and Huber, 1991).

found that HET-S is able to delay the onset of fibrillization in substoichiometric ratios as low as 1:700 (HET-S: PFD). The results plotted in Figure 1B show that at a ratio of 1:70, the onset of aggregation is delayed by several hours yet still proceeds relatively quickly once it begins. At the 1:7 ratio, the aggregation is delayed by more than 65 hr but eventually occurs sometime before 110 hr (data collection was not continuous after 24 hr). As expected, the addition of HET-s at substoichiometric ratios (up to 1:7) does not have an inhibitory affect. Also, HET-S (1–227) does not significantly inhibit at a 1:7 ratio, thus demonstrating that the PFD of HET-S is required for the in vitro inhibition of PFD aggregation in *trans* (data summarized in Table S1, available online).

Structural Composition of HET-s and HET-S

Having demonstrated that the HET-S prion-inhibitory effect is an intrinsic property of the protein, we set out to determine the structural basis of this functional difference between the HET-s and HET-S proteins. We have previously shown that the HET-s in its soluble form is composed of an N-terminal folded domain comprising residues ~1–227 followed by a flexible and highly dynamic C-terminal tail (Balguerie et al., 2003). Since HET-S differs from HET-s in only 13 out of its 289 residues, it is not surprising that we find the same domain composition for HET-S. As in the case of HET-s, the [^{15}N,^{1}H]-TROSY spectrum of HET-S has two qualitatively different kinds of peaks: a first group of about 220 broad cross peaks with full line widths at half height along ^{1}H of ~25 Hz and a second group of about 70 sharp, more intense cross peaks with line widths of ~14 Hz indicative of amino acid residues in a flexible conformation. Comparison with the [^{15}N,^{1}H]-TROSY spectrum of HET-S(1–227) (Figure S1) shows that the first group of peaks has their counterpart in HET-S(1–227). We established the sequential assignment of HET-S, and the ^{13}Cα chemical shifts are consistent with these domain boundaries: the per-residue chemical shift deviation of HET-S (Figure S2) shows that it is composed of an N-terminal mostly helical structured domain comprising at least residues 13–222 followed by an unstructured and flexible C-terminal tail. In addition to having near-random coil ^{13}Cα chemical shifts, the C-terminal tails of both HET-S and HET-s are highly dynamic as evidenced by low ^{15}N{^{1}H}-NOE values (Figure S3).

Structure of the HET-s Globular Domain

The structure of HET-s(1–227) was solved by heavy atom phasing, and the refined coordinates were used as a starting model for the structure determination by molecular replacement of HET-S(1–227) and of HET-s[D23A,P33H](13–221), the globular domain of a mutant that exhibits the [Het-S] phenotype in vivo (structure factors and coordinates were deposited in the Protein Data Bank, see Table 1). All three proteins contain the same α-helical fold of 8–9 helices with a short two-stranded β sheet (Figure 2). The first helix, α1 (residues 2–8) is only visible in the HET-S crystals. Its absence in the HET-s structure may be a crystallographic artifact, and the HET-s[D23A,P33H](13–221) construct lacks the residues that make up this helix. This shorter construct was designed based on the defined regions in the

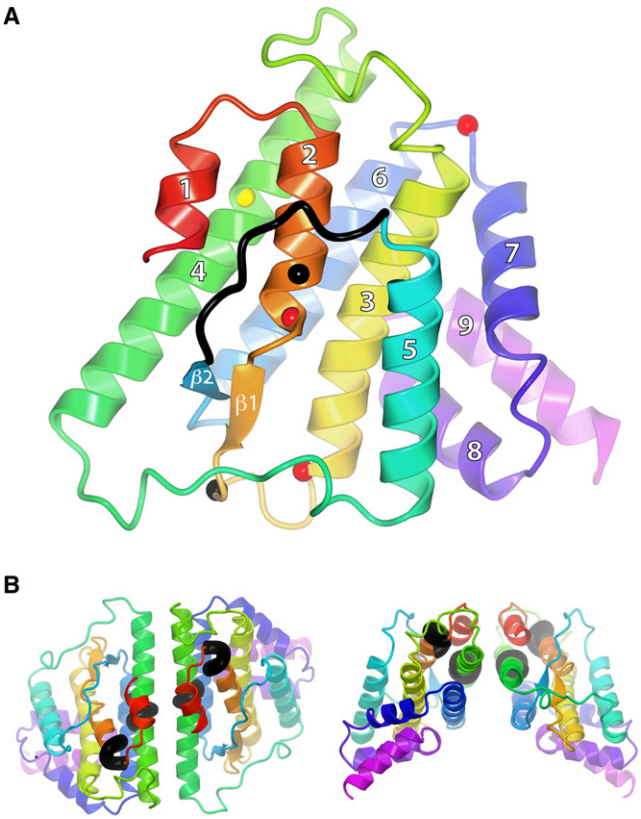

Figure 2. The Structure of the HET-S N-Terminal Domain

(A) Ribbon diagram of HET-S(1–227). The ribbon color is a rainbow gradient from N (red) to C terminus (purple). Regions of the molecule are highlighted as follows: flexible loop L5-6 in black, residues A23 and H33 as black spheres, location of point mutants that can convert HET-S to [HET-s] phenotype as red spheres, and residue E86 as yellow sphere. The helices are numbered 1–9 and β1–β2 for the strands.

(B) Perpendicular views of the crystallographically observed HET-S(1–227) dimer with consensus residues from the β-aggregation prediction algorithms (see the Experimental Procedures) as black tubes.

initial structure determination of HET-s(1-227), in an effort to improve the diffraction by crystallizing a protein without the flexible ends. Indeed, it did yield the best diffracting crystals (Table 1), although the construct itself is significantly less stable (see below). The first five helices of HET-S pack in a regular antiparallel bundle followed by a loop and short β strand that connects α5 and α6. This loop (L5-6) comprising residues 137–147 and strand β2 thread back through the molecule (between α2 and α4) so that α5 and α6 are parallel but on opposite sides of the molecule. The last three helices (α7–α9) form a three-helix bundle substructure that packs approximately perpendicular to the first six helices. The overall shape of the fold is roughly an equilateral triangle of ~55 Å on a side and a thickness of ~25 Å.

There are to date more than 30 homologs of the HET-s N-terminal globular domain that can be identified with a PSI-BLAST search, all of which come from filamentous fungi and none of which have a known function (Figure S4). One of the homologs was identified in a screen for mutants that affect the pathogenicity of *Leptosphaeria maculans*, the fungus that causes blackleg disease of *Brassica napus* (rapeseed). This loss-of-pathogenicity (LOP-B) protein has 529 amino acids, and its N terminus is 31% similar to the HET-s globular domain. Henceforth, we refer to this particular fungal domain with its helical fold as the HeLo domain (HET-s/LOP-B). The conserved residues of the HeLo domain correspond primarily to buried residues in the HET-S(1–227) structure. The lack of surface-exposed residue conservation suggests that the fold is well conserved but that the function or target of the domain may differ among the HeLo domain-containing proteins. The degree of conservation is highest in the first ~60 residues, with little or no conservation in the loops between secondary structures. The sequence of the last ~50 residues, comprising the three terminal helices, is less well conserved (Figure S4).

Comparison of the HeLo Domain Structures of HET-s and HET-S

Despite the fact that all three constructs were crystallized in diverse conditions with different numbers of molecules in their asymmetric units (Table 1), they exhibit only minor differences. An overlay of HET-s and HET-S gives a root-mean-square deviation (rmsd) of 0.82 Å (0.81 Å for chain B) for the main-chain atoms in residues 11–223. For comparison, the overlay of chain A and B of HET-S within the same crystal gives an rmsd of 0.31 Å. Overlays of HET-s[D23A,P33H] with HET-s and HET-S give similarly low numbers. Hence, the structures are so similar that local differences need to be interpreted carefully, taking into account possible crystal packing effects. The first major difference between HET-s and HET-S is the N-terminal helix α1 that is present only in HET-S. However, the solution NMR spectra of neither HET-S nor HET-s indicate the presence of helix α1 in solution: the $^{13}C\alpha$ and $^{13}C\beta$ chemical shifts for the residues in this region do not exhibit helical deviations from their random coil values (Figure S2). Furthermore, we could not detect a difference in the helical content of the two proteins by CD spectroscopy (data not shown). There are two factors that may explain the discrepancy between the crystal structures and solution structures: (1) Since helix α1 resides at the dimer interface, it may not be stable in the monomeric form. If so, the 0.5–1 mM protein used for the NMR measurements may have led to an insufficient dimer population to support the helix (note that the crystals contain 15–20 mM protein). (2) The crystallization conditions of HET-S (4.0 M NaCl) may have stabilized the hydrophobic interaction that the helix α1 makes with itself at the interface, while the low salt conditions for HET-s (30% PEG 4000, ~100 mM NaCl) may have had less of a stabilizing influence. The helix is necessarily absent from the mutant structure because it is not in the construct that was crystallized (residues 13–221). Therefore, we cannot conclude from the crystal structures that helix α1 is unique to HET-S, but it appears to be a quasistable structure that is absent from both HET-S and HET-s in solution.

The second major structural difference occurs in the loop L5-6, the residues of which have higher B factors and are generally less well ordered than the other loops (Figure 2A and Figure S5). In the case of chain B from the mutant, its electron density is too weak to be confidently modeled. In HET-s there is a salt bridge between K145 of the loop L5-6 and D23 of helix α2 that stabilizes

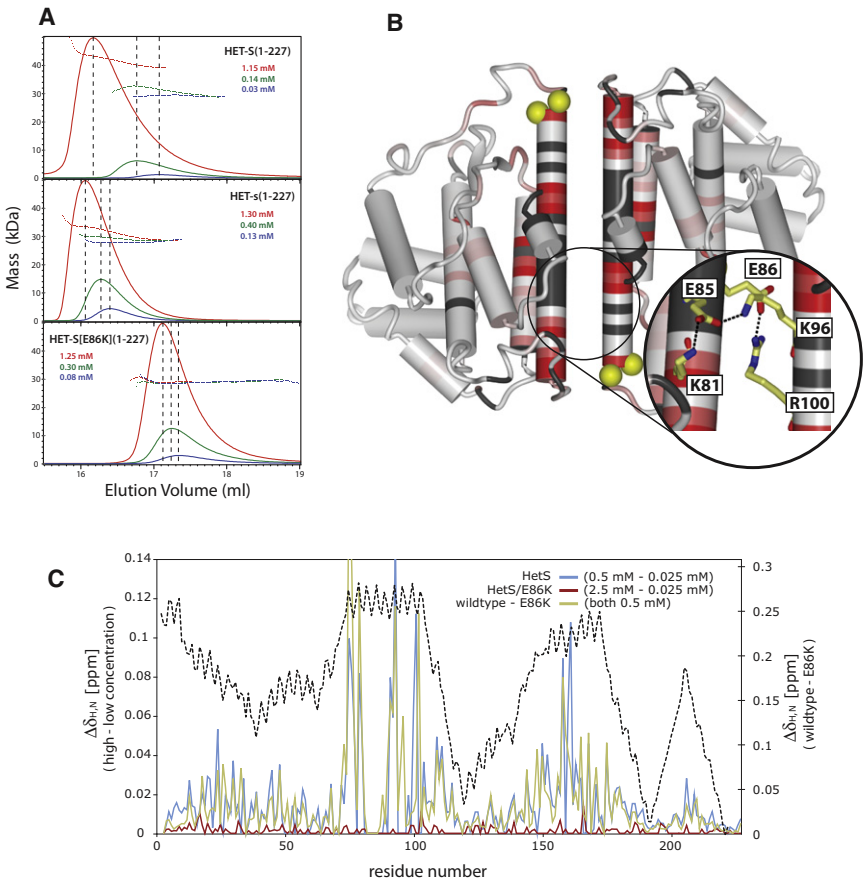

Figure 3. The HET-S Solution Dimer Shares the Same Interface as the Crystallographic Dimer

(A) Gel filtration and MALS profiles reveal the presence of a dimer of HET-S in solution. The proteins were injected onto the sizing column at the three concentrations indicated, and the eluted proteins were simultaneously analyzed for concentration (solid lines) and molecular weight (dotted lines). The vertical dashed lines indicate the elution volume. The concentration-dependent peak broadening, elution time, and calculated mass of HET-S compared to HET-S[E86K] all indicate that the former self-associates in solution.

(B) The weighted chemical shift differences ($\Delta\delta_{H,N}$) between the highest and lowest concentrations (see Figure S6) were mapped to the 3D structure of HET-S(1–227) as a gradient of white ($\Delta\delta_{H,N}$ < 0.02 ppm) to red ($\Delta\delta_{H,N}$ > 0.08 ppm) with unassigned residues in dark gray. The circle inlay highlights the charged residues at the interface near E86.

(C) Per residue plot of the concentration-dependent $\Delta\delta_{H,N}$ (2.5 mM–25 μM) for HET-S[E86K](1–227) and (500 μM–25 μM) for HET-S(1–227) and the isoconcentration $\Delta\delta_{H,N}$ for HET-S(1-227) wild-type versus the mutant (500 μM). The isoconcentration $\Delta\delta_{H,N}$ is plotted on a separate y scale (~40%) to make a better comparison of the per residue shift pattern. The missing assignments appear as gaps in the plot. The dashed line represents the distance of each Cα to the interface with shortest distances nearest the top, showing the inverse correlation between distance from interface and $\Delta\delta_{H,N}$.

the loop conformation, while for HET-S and the mutant this interaction is absent (Figure S5B). HET-S and the mutant have an alanine at position 23, and L5-6 in their structures adopts a slightly more open conformation, moving 2–4 Å away from α2.

In the HET-S(1–227) and HET-s[D23A,P33H](13–221) crystal structures, the residual B factors for α7-α9 are higher than those for α1-α6 (Figure S5C). In the HET-s structure these three helices do not have heightened B factors, but their lower sequence conservation is indicative of a somewhat independent structural unit. Although none of the structures was solved at atomic resolution, precluding an anisotropic refinement of the B factors, there was evidence of anisotropy in the molecule. We refined the models with the inclusion of four TLS (translation, libration, screw) domains, which led to a significant lowering of the crystallographic R factor R_{free} (0.7%, 1.8%, and 2.4% for HET-s[1–227], HET-s[D23A,P33H][13–221] and HET-S[1–227], respectively).

The Crystallographic Dimer Is Also Present in Solution

In the three structures reported here as well as every other crystal form of the different HET-s constructs that we obtained (total of 12 asymmetric molecules in 5 crystal forms), the crystal packing incorporated a common 2-fold symmetric dimer that was related by either crystallographic symmetry or by proper noncrystallographic symmetry (Figure 2B). Due to their poorer data quality, the other crystal forms were not pursued once they were solved by molecular replacement and are not discussed further here. The HET-S dimer interface consists of an equal amount of charged and nonpolar residues (nine residues or 39%) and has a moderate surface area of 944 Å^2 (863 Å^2 for HET-s; smaller due to lack of α1). During purification of these molecules on a Superdex 75 gel filtration column, their elution volumes were more consistent with their being monomeric based on calibration with globular proteins. However, the ubiquitousness of the dimer in the crystals led us to investigate whether it also existed in solution.

To test the oligomerization state of the different HET-s constructs, we measured the masses of the solution species by multiangle light scattering (MALS) coupled to the flow from a G2000SWXL gel filtration column. By injecting protein at concentrations ranging from 25 to 2300 μM, we observed varying degrees of partitioning between a monomer and dimer (Figure 3A). The association constant of the dimer is low enough that there is significant dissociation during the dilution and separation that occurs on the column, resulting in a single peak. However, at higher protein concentrations there is a clear decrease in mass from the start to the end of the peak with a concomitant broadening and decrease in retention time. Although such a low-affinity interaction does not at first appear to be biologically relevant, the fact that HET-s and possibly HET-S can oligomerize via their C-terminal PFDs implies that the N-terminal domain might also oligomerize at the high local concentration that exists in a fibrillar state (see below).

An interesting mutant of HET-S (E86K) that was found in a genetic screen (Coustou et al., 1999) unexpectedly relates to the dimer. When expressed in *P. anserina*, HET-S[E86K] gives rise to a neutral phenotype that is reactive with neither [Het-s] nor [Het-S] phenotypes yet retains the ability to transmit the infectious prion state of [HET-s]. This means that a HET-S[E86K]-expressing strain that is confronted with a [Het-s] strain can subsequently convert a colony from a [Het-s*] to a [Het-s] phenotype. The E86K mutation occurs at the center of the dimer interface (Figure 3B), disrupting a salt bridge, several hydrogen bonds, and much of the charge complementarity of the interface. Indeed, GFC-MALS measurements of HET-S[E86K](1–227) show that up to the highest concentration injected (2.3 mM) no dimers are detected. Furthermore, HET-S[E86K] gives rise to significantly sharper lines in [^{15}N,^{1}H]-TROSY spectra than HET-S (see below). However, we wanted to confirm the importance of the dimer for HET-S activity, and so we attempted to restore the dimerization of HET-S[E86K] via a complementary mutation. Although we failed in the attempt, we found that another charge-altering mutant at the interface (R100E) also destroys the solution dimer (data not shown). Transformation of *P. anserina* with this mutant yielded fungi lacking the [Het-S] phenotype but able to propagate the infectivity as observed with the original E86K mutant. In addition, a fraction of the transformants even gave an incompatibility reaction when confronted with [Het-S] strains and thus acquired a full [Het-s] phenotype. Thus, these mutations that lie in the middle of the crystallographically observed dimer interface disrupt the dimer formation in solution and inactivate the [Het-S] phenotype, yielding strains that are able to propagate the [Het-s] prion form. Although this is very suggestive of a biological role for the dimer, it is still indirect evidence, as the loss of the dimer could be peripheral to the loss of function.

To further verify that the dimer interface in solution is the same as that seen in the crystal structures, we measured the concentration dependence of the chemical shifts in the [^{15}N,^{1}H]-TROSY spectra of the protein constructs. The backbone chemical shift assignments for the N-terminal domains (>95% complete) were made by standard approaches (see the Experimental Procedures). Using the lowest and highest concentrations measured for HET-S(1–227), we mapped the weighted chemical shift differences ($\Delta\delta_{H,N}$) for each residue onto the structure. The results depicted in Figures 3B and 3C indicate a strong correlation between chemical shift perturbation and the proximity of a residue to the crystallographically observed interface. Thus, the dimer in solution has the same interface as in *crystallo*. The concentration dependence of the chemical shifts (Figure S6) indicates that the monomer-dimer equilibrium is in the fast chemical exchange regime. In agreement with the MALS data, the spectra collected for HET-S[E86K](1–227) do not exhibit any significant concentration-dependent chemical shifts up to 2.5 mM protein, whereas those for HET-s(1–227) do. The concentration-dependent $\Delta\delta_{H,N}$ for HET-S and the isoconcentration (0.5 mM) $\Delta\delta_{H,N}$ between the E86K mutant and the wild-type protein exhibit a similar residue-specific pattern (Figure 3C). Thus the E86K mutant appears to represent the pure monomer state of the protein. We fit the concentration-dependent $\Delta\delta_{H,N}$ values to a monomer-dimer equilibrium model (see the Supplemental Experimental Procedures) to obtain an estimate of the dimer affinity. For HET-S, the fit of 20 peaks at 4 concentrations (25, 100, 270, 540 μM) gave a K_D of 78 ± 15 μM and for HET-s using 10 peaks at 5 concentrations (25, 125, 500, 1000, 2500 μM) gave a K_D of 320 ± 37 μM.

HeLo Domain and PFD of Neither HET-s nor HET-S Interact in Their Soluble Forms

One hypothesis as to why HET-s but not HET-S can form a prion would be that there is an inhibitory interaction between the tail (PFD) and the head (HeLo domain) in HET-S, which precludes incorporation of the PFD into a fibril. We searched for evidence of such an interaction using the following NMR-based experiments: (1) Chemical shifts very sensitively probe the structural environment. Hence, a comparison between the chemical shifts of HET-S(1–227), HET-S(218–289), and HET-S, as well as the corresponding HET-s constructs, should give insights into the possible interactions. For a residue-resolved analysis, the backbone resonances of HET-S and HET-s, as well as those of their isolated HeLo domains, were assigned. This analysis revealed that no ^{15}N-^{1}H moieties exhibit a significant difference in chemical shifts between the full-length constructs and their respective 1–227 or 218–289 constructs (data not shown). (2) The chemical shifts of ^{15}N-labeled HET-s(218–289) were monitored upon addition of several-fold excess of unlabeled HET-s(1–227) or HET-s[D23A,P33H](1–227), the mutant that mimics the HET-S phenotype. Despite adding an excess of the HeLo, no chemical shift changes on the PFD domain were observed (data not shown). (3) Since an interaction of the flexible PFD would decrease its highly dynamic nature, we measured the ^{1}H-^{15}N heteronuclear NOEs (^{15}N{^{1}H}-NOE) (Kay et al., 1989) for HET-s and HET-S. Similar ^{15}N{^{1}H}-NOE profiles were obtained (Figure S3) indicating that both proteins have the same degree of flexibility in their C-terminal domains, consistent with the high degree of similarity in the chemical shifts for the PFD residues of HET-s and HET-S (Figure S7). The three-dimensional structure of the isolated HET-s PFD in its fibril form (Wasmer et al., 2008) suggests that the terminal tryptophan residue plays an important role in the growth of the fibrils. So, despite the previous negative results, we hypothesized that this aromatic residue may bind back onto a region of the globular domain of HET-S in order to inhibit spontaneous fibril growth. (4) Thus a saturation transfer difference NMR experiment (Mayer and Meyer, 2001) was measured to detect a potential interaction by ^{1}H-^{1}H cross-relaxation from W287 to the HeLo domain of the protein, yet no magnetization transfer was observed (data not shown). (5) To exclude the possibility that interference from the C-terminal histidine tag was masking a "head-tail" interaction in the above experiments, the chemical shifts of a nontagged HET-S were compared with the HET-S construct measured above. In addition, a ^{15}N-resolved [^{15}N,^{1}H]-HSQC-NOESY experiment with long mixing time was executed on this nontagged HET-S protein. Neither considerable chemical shift differences nor NOEs between the flexible PFD and the structured HeLo domain were observed (data not shown), further supporting the lack of transient interactions between these domains. Our failure to detect an interaction is not likely an artifact of the buffer used, since they were close to physiological conditions, and experiments (1) and (2) were measured in various buffers (phosphate,

Tris-HCl) within a pH range of 6.5–8 and by varying the NaCl concentration between 50 and 200 mM. In summary, we failed to show (transient) interactions between the C-terminal PFD and the N-terminal HeLo domain of HET-S and therefore reject the hypothesis that such an interaction could account for the prion-inhibitory activity of HET-S.

HET-s Is Thermodynamically More Stable Than HET-S

The thermodynamic stability of several constructs was probed by temperature-induced unfolding monitored by circular dichroism (CD) spectroscopy. The isodichroic point at 201 nm throughout the measurements suggests that the thermal denaturing of HET-s is a simple two-state process (data not shown), and for all of the constructs tested, we observed a single unfolding transition. The T_m, or midpoint of the transition, was derived by fitting the data to a two-state unfolding model (see the Experimental Procedures). The T_m for HET-S(1–227) was found to be 48°C compared to 57°C for HET-s(1–227) (Figure 4). The N-terminal domain of HET-s[D23A,P33H], the [Het-S] specificity mutant, has a T_m that is 5°C lower than HET-s, indicating a correlation between the stability of the N-terminal domain and its associated phenotype (arrow 1). Shortening the construct to HET-s[D23A,P33H](13–221) lowered its T_m to 43°C (arrow 2). In contrast, the presence of the PFD has a minimal effect on the thermal stability of the protein constructs, lowering the melting temperature by 1°C compared to the isolated HeLo domains (data not shown). The HET-S[E86K] mutant that gives rise to the compatibility phenotype in vivo is 3°C more stable than HET-S (arrow 3). This increase in stability is not likely due to a monomer versus dimer stability difference, since the concentration at which the measurements were performed (10 μM) favors monomer for all of the constructs. These analyses reveal that in spite of their structural similarities, HET-s and HET-S differ significantly in terms of thermodynamic stability. Furthermore, the HET-s[D23A,P33H] and HET-S[E86K] mutants show that there is a correlation between the thermodynamic stability of the protein and the phenotype that it exerts.

HET-S Can Associate to HET-s Aggregates In Vivo, and β-Breaker Mutations in the C-Terminal Region of HET-S Neutralize [Het-S] Activity In Vivo

A previous study showed that constitutive coexpression of HET-s and HET-S in a single fungus led to a metastable strain that displayed at times both normal and restricted cell growth (Coustou-Linares et al., 2001). This instability is probably due to a balance between the cell death reaction and prion elimination activity of HET-S (Coustou et al., 1999; Coustou-Linares et al., 2001). Because of the experimental setting used in that study, direct interaction of HET-S with HET-s prion aggregates could not be monitored, so we generated strains that coexpress HET-s-RFP and HET-S-GFP. As seen previously, expression of HET-S-GFP alone leads to diffuse cytoplasmic fluorescence and HET-s-RFP to the formation of dot-like aggregates (data not shown). Strains that coexpressed HET-s-RFP and HET-S-GFP displayed various degrees of growth defects with a partial inhibition of HET-s-RFP dot-like aggregate formation, a situation already described in the previous study. However, where

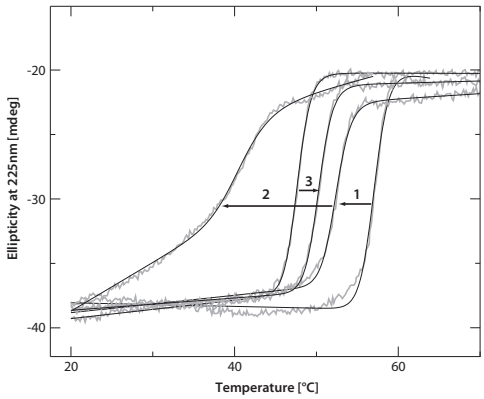

Figure 4. HET-s Protein Constructs Are More Stable than HET-S

Overlay of the CD thermal denaturation profiles (gray lines) and their fits (black lines) for the N-terminal domain constructs. The arrows indicate the effects of the mutations or changes in the domain boundaries: (1) HET-s→HET-s [D23A,P33H]; (2) HET-s[D23A,P33H] (1–227)→(13–221); (3) HET-S→HET-S [E86K]. From low to high thermal denaturation temperature, the traces correspond to HET-s[D23A,P33H](13-221), HET-S(1-227), HET-S[E86K](1-227), HET-s[D23A,P33H](1-227), and HET-s(1-227).

present, HET-s-RFP aggregates invariably contained HET-S-GFP signal as well (Figure 5).

Since the C-terminal domain of HET-S is necessary for HET-S activity in vivo (Balguerie et al., 2003) and HET-S interacts with HET-s aggregates in vivo, we hypothesized that the interaction of HET-S with the HET-s prion involves a β-structuring of the PFD of HET-S into the β-solenoid fold of the HET-s fibril. In the initial structural characterization of the HET-s prion, the in vivo effect of several HET-s constructs containing small deletions in the PFD or point mutants that substituted a proline for a residue of the PFD were tested (Ritter et al., 2005). The deletion and proline mutants that resided in and hence disrupted the β-solenoid amyloid core led to loss of [Het-s]. Using the same set of mutants that identified the β-structured regions of the HET-s prion, we examined the role of the HET-S PFD on the activity of HET-S in *P. anserina*. As summarized in Figure S8 and detailed in Table S2, the exact same proline and deletion mutants that were previously found to disrupt the HET-s prion also led to null mutants in HET-S while those that did not disrupt HET-s function also had no affect on HET-S. These genetic results strongly suggest that the PFD of HET-S must be able to adopt the β-solenoid prion-like fold in order for it to exert its prion-inhibitory and incompatibility activity in vivo.

An Insertion Mutant of HET-S Lacking Overlap between the HeLo Domain and the PFD Is a Prion and Loses [Het-S] Activity

The experimentally determined domain boundaries for the HeLo domain and PFD slightly overlap (1–227 and 218–289, respectively), and it was shown that the structuring of the PFD upon fibril formation leads to some unfolding of the globular domain in HET-s (Wasmer et al., 2009). Considering the decreased thermodynamic stability of HET-S compared to HET-s, we hypothesized that this coupling between PFD folding and HeLo domain unfolding might be even more pronounced in the case of

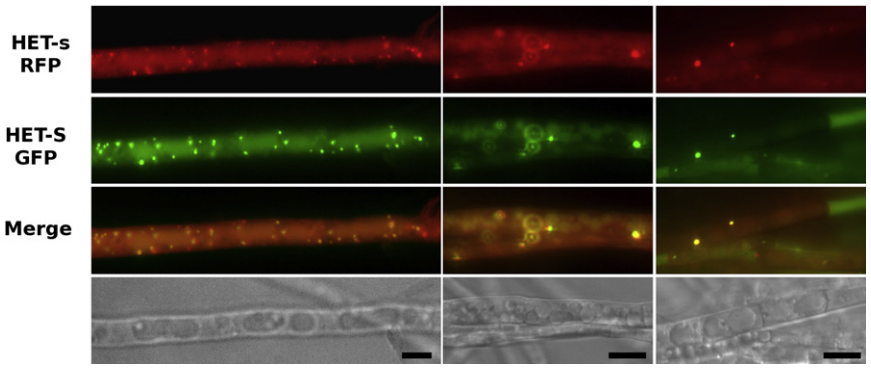

Figure 5. HET-S Can Associate with HET-s Aggregates In Vivo

A *P. anserina* strain coexpressing HET-S-GFP and HET-s-RFP was analyzed by fluorescence microscopy. The hyphae of the transformants displayed various degrees of growth alteration and in the three fields shown, strong vacuolisation and formation of lipid droplets, the hallmarks of incompatibility. Where HET-s-RFP aggregates are visible, HET-S-GFP signal is also detected. Scale bar is 4 μm.

HET-S and be directly involved in the prion-inhibitory effect of the HET-S HeLo domain. We thus set out to uncouple the HeLo domain from the PFD β-solenoid conformation (i.e., fibril formation) by removing the overlap between them. The result is a construct designated HET-S$^{(1\text{-}227)(218\text{-}289)}$ that corresponds to the HET-S globular domain (1–227) fused to the PFD region (218–289) with a six amino acid linker between the two domains. A plasmid expressing the HET-S$^{(1\text{-}227)(218\text{-}289)}$ construct was introduced in a *Δhet-s* strain, and transformants were tested for their ability to be infectious (propagate [Het-s]) and for their compatibility with *het-s* and *het-S* strains. Strains expressing HET-S $^{(1\text{-}227)(218\text{-}289)}$ were compatible with [Het-s] strains, meaning that they have lost HET-S activity. After confrontation with [Het-s] strains, the same transformants became capable of subsequently converting [Het-s*] strains to the [Het-s] phenotype. In other words, the HET-S$^{(1\text{-}227)(218\text{-}289)}$ construct is capable of prion propagation. A small fraction of the transformants produced an attenuated incompatibility reaction with [Het-S] strains, indicating that HET-S$^{(1\text{-}227)(218\text{-}289)}$ has some but not all the activity of HET-s (Table S3). Taken together, these results suggest that when the globular domain of HET-S becomes structurally uncoupled from the C-terminal PFD, its prion-inhibitory activity is abolished.

DISCUSSION

The Prion Inhibition Mechanism of the HeLo Domain of HET-S

In the original description of the [Het-s] system it was found that HET-S has the ability to inactivate [Het-s] (Rizet, 1952). The [Het-s*] state was first obtained by curing of the prion by interaction with a [Het-S] strain, and the original nomenclature of the [Het-s*] state was actually s^S to emphasize that the infectious element had been modified/inactivated by HET-S. Later, it was shown that this prion-inhibitory effect is also exerted in *cis*, so that the HET-S globular domain inhibits the PFD present in the HET-S protein (Balguerie et al., 2003). The question arises as to how the HeLo domain of HET-S can exert this prion-inhibitory effect. We show that in vitro, HET-S fails to form well-ordered fibrils and inhibits fibrillization of the HET-s PFD, hence providing a direct illustration of this prion-inhibitory effect. We could find no evidence of an interaction between the HeLo domain and the unstructured, flexible PFD in HET-S. Furthermore, single-point mutations that switch the phenotype in both directions (Coustou et al., 1999) are distributed all over the 3D structure of the N-terminal domain (Figure 2A), making it difficult to imagine how a specific binding epitope for the PFD exists on HET-S that is absent on HET-s.

We did find that one striking difference between HET-s and HET-S HeLo domains resides in their thermodynamic stability. We also show that HET-S activity relies on the ability of its PFD to adopt the β-solenoid fold characteristic of the HET-s prion. Based on our new data, and the HET-s literature to date, we propose a model for the prion regulation by HET-S that explains both the *cis* and *trans* prion inhibition (Figure 6). Since the aggregation of the HET-s PFD into fibrils displays the complex kinetics of a seeded polymerization (Sabate et al., 2009), the formation of a seed aggregate that will subsequently lead to a mature fibril is a necessary first step in the aggregation process. In the proposed model, the acquisition of the β-solenoid fibril fold by the PFD in HET-s does not grossly destabilize its HeLo domain, whereas in HET-S the spontaneous (*cis*) or HET-s fibril-induced (*trans*) β-solenoid folding of the HET-S PFD leads to a more extensive structural rearrangement of the HET-S HeLo domain that renders the seed or fibril sterile for further fibril growth. Although we do not know the precise nature of the change that is induced in the HET-S HeLo domain, it likely involves a degree of unfolding (Wasmer et al., 2009), perhaps exposing some prion-inhibitory and/or cytotoxic elements.

We have shown by uncoupling the PFD from the HeLo domain that their overlap is essential to the in vivo properties of HET-S (Table S3). The reported loss of structure in the fibrils of HET-s (Wasmer et al., 2009) is particularly evident for the residues in the last three helices (α7–α9), the same for which we find increased residual B factors in HET-S. In addition to its lower stability, the HET-S HeLo domain is more aggregation prone. Under moderate agitation, HET-S(1–227) precipitates at room temperature within a few hours, while HET-s(1–227) remains in solution under the same condition for more than a week (data not shown). Furthermore, three independent algorithms that predict β-aggregation prone regions in HET-s and HET-S (see the Experimental Procedures) gave high scores for several regions within the HeLo domains of both proteins. Interestingly, the consensus predictions cluster at the dimer interface (Figure 2B). The forced proximity of HeLo domains in the β-solenoid seeds or fibrils would support the formation of the low-affinity (~80 μM) HET-S dimer, thus juxtaposing aggregation-prone regions that could facilitate an aggregation of the HeLo domains. Either the

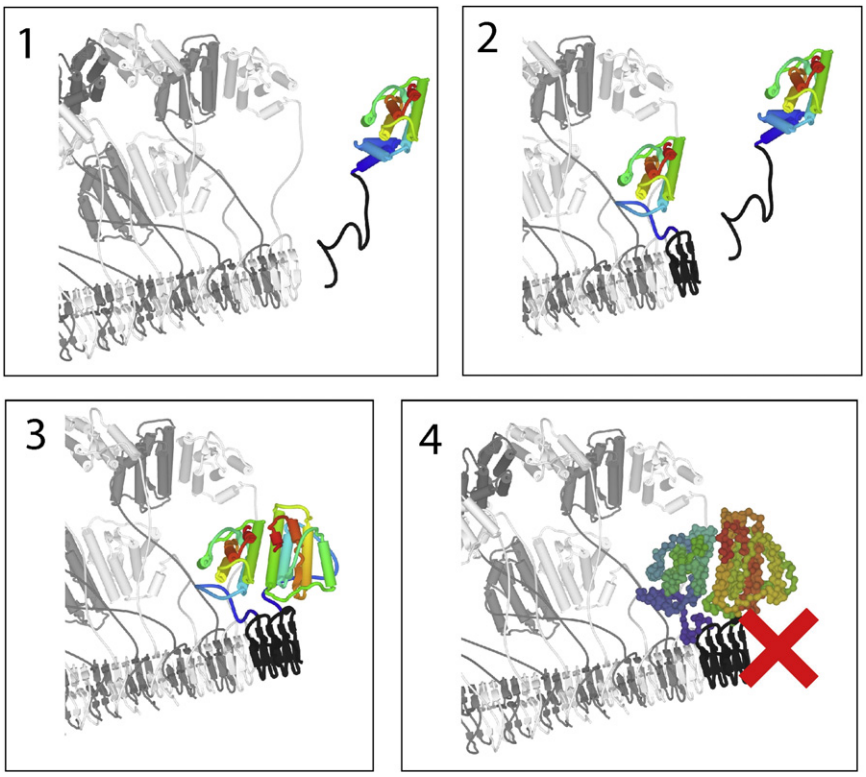

Figure 6. Proposed Model for HET-S Fibril Inhibition and Induction of Toxicity

(1) The HET-s fibril (formed from alternating light/dark gray HET-s monomers) is approached by a soluble HET-S (rainbow HeLo domain with random coil PFD in black). (2) Upon addition of HET-S to the HET-s fibril, the terminal helices of its HeLo domain unwind to accommodate the prion fold. (3) The second addition of a HET-S monomer to the fibril leads to a dimerization of the HeLo domains which facilitates a re/unfolding of the HeLo domains with the potential for further aggregation of HeLo domains that (in 4) blocks further growth of the fibril and activates a toxic form of HET-S. The model for the HET-s fibril was created from the PFD fibril structure (Wasmer et al., 2008) and the HeLo domain with an unwinding the last three helices of the HeLo domain (residues 177–222) to make space for the HeLo domains around the fibril. The HET-s HeLo domains are depicted as dimers between adjacent monomers in the fibril, but these are speculative and it should be emphasized that the structures of the HeLo domains of HET-s and HET-S, in the context of a fibril, are not known except that HET-s suffers a loss of tertiary structure (more molten globule-like), with a local loss of secondary structure around residues 190–220 (Wasmer et al., 2009).

fibril-induced dimer or the resulting aggregates could interfere with further fibrillar aggregation via the PFDs. Since we cannot rule out that to some extent the HeLo domain refolds in order to attain its functions, we refer to the change induced in the HET-S HeLo domain by its PFD structuring as a "re/unfolding."

Our model depicted in Figure 6 distills these findings into an inhibition mechanism in which the lower thermodynamic stability and higher aggregation propensity of the HET-S HeLo domain are key to its prion regulation mechanism: when its PFD acquires the β-solenoid fold, either through the kinetically slower process of spontaneous seed formation or upon binding to the β-solenoid fibrils of HET-s, it re/unfolds to yield "seedless aggregates" that are incompetent for continued fibrillar growth. This model further explains why the HET-S mutations that prevent formation of the β-solenoid fold in its PFD abolish HET-S activity. The re/unfolding of the HeLo domain is not simply a consequence of the β-folding of the PFD but is due to a structural overlap between the two domains.

Potential Role of the HET-S Dimer and Its Aggregation in Heterokaryon Incompatibility

The heterokaryon incompatibility reaction of the HET-s/S system involves a spatially restricted PCD that requires the presence of both HET-s fibrils and soluble HET-S, while no reaction occurs in presence of soluble HET-s and HET-S (Coustou et al., 1997). This suggests that either (1) a poisonous HET-S entity is induced by HET-s fibrils or that (2) a poisonous complex forms between HET-S and HET-s fibrils. The prion inhibition model proposed above supports these mechanisms of toxicity: (1) the HET-s fibrils induce a partial unfolding of HET-S by binding to and structuring its PFD domain, thus generating a toxic HET-S entity, or (2) the ability of HET-S to prevent the growth of HET-s fibrils promotes the formation of a toxic oligomeric species similar to other amyloid oligomers in neurodegenerative diseases (Glabe, 2006).

Although the area of the dimer interface is not enormous, its size is consistent with protein-protein interaction surfaces, and it is predicted to be a stable interface in solution by the PISA algorithms (Krissinel and Henrick, 2007). We find that two different interface mutants that disrupt the in vitro dimer also disrupt the in vivo functions of HET-S. We have also shown that the E86K mutant loses the prion-inhibitory function of HET-S in vitro (Figure 1B, Table S1). Thus it appears that the interface could be important for both toxicity and prion inhibition. It is tempting to say that the dimer interface also plays a role as an aggregation or re/unfolding facilitator in the prion inhibition mechanism discussed above (Figure 6); however, the dimerization and the re/unfolding are not linked experimentally and are rather two possible explanations for the properties of HET-S.

In the simplest model, the re/unfolded HeLo aggregate is the toxic entity in the incompatibility reaction. Such a mechanism of toxicity ensures that HET-S alone cannot form sufficient aggregates to be toxic because its physiological concentration precludes dimer formation and it cannot make its own unfolding machinery (i.e., the HET-s fibril). If the HeLo domain actually is a fungal cell death-inducing domain, then the β-folding of its associated PFD would also represent the trigger for its activation. In this scenario, the two biological properties of HET-S (its

ability to induce cell death upon interaction with the HET-s prion and its ability to cure [Het-s]) would be based on the same mechanistic principle involving a structural alteration of its HeLo domain. We currently believe this to be the case, but a conclusive answer is the topic of further study in our lab.

Conclusion

Prions have the unique ability to encode their function as well as their replication features within their 3D structures. HET-s adds to the unusual repertoire of prions in that in addition to its nontoxic monomeric and propagative structural entities, there are prion-regulatory and toxic structural entities, all of which are encoded in two highly homologous proteins HET-S and HET-s. While the 3D structure of the HET-s(218–289) fibrils shed light on the mechanism of prion formation and propagation (Wasmer et al., 2008; Ritter et al., 2005), the presented 3D structures of both soluble HET-S and HET-s indicate that the mechanism of prion regulation is coded in the stability of the N-terminal domain rather than in its structure, while the generation of toxicity may be based on an activation of the HeLo domain triggered by β-folding of the C-terminal PFD.

EXPERIMENTAL PROCEDURES

HET-s Constructs and Expression

All of the proteins were expressed as either N-terminal 6-histidine tag (N6His) fusions with a thrombin cleavage site or as C-terminal (C6His) fusions with no intervening sequence, and expressions were carried out in *E. coli* strain BL21-DE3(pLysS) grown in M9 minimal medium. The details of the expression and purification are in the Supplemental Experimental Procedures.

Mass Analysis by GFC-MALS

The pure proteins in gel filtration buffer were concentrated with centrifugal ultrafiltration devices to ~2.3 mM and then serially 2× diluted to make a series that extended to ~80 μM. The protein solutions were separated by size with a G2000SW$_{XL}$ gel filtration column (Tosoh Bioscience) in 20 mM Na_2HPO_4/KH_2PO_4 (pH 7.0), 200 mM NaCl on an Agilent 1200 series HPLC system injected by the autosampler (20 μl) at a flow rate of 0.5 ml/min. The column eluate was simultaneously monitored by the 1200 series diode array detector, a TREOS light-scattering detector (Wyatt Technology), and the 1200 series refractive index detector. The signals from the detectors were analyzed by the Astra V program (Wyatt Technology) using either the calculated extinction coefficients or an average protein dn/dc value of 0.187 ml/g. Both concentration measurements (UV or RI) gave similar calculated masses.

Crystallization, Structure Determination, and Refinement

Crystals were first obtained for HET-s(1–227) without a histidine tag in 0.2 M $(NH_4)_2SO_4$, 0.1 M Tris (pH 8.5), 30% PEG 4000 in the spacegroup p3121, and initial phases were obtained to 3.5 Å by SAD and MAD techniques using SHARP (de la Fortelle and Bricogne, 1997) with mercury and iodine derivative data sets (single wavelength collected on beamline 7.2 at SSRL) in combination with a three-wavelength data set from a bromine-soaked crystal (beamline 8.2.1 at ALS). The highest-resolution native data obtained with these crystals were to 3.0 Å, and so we searched for other crystal forms. The statistics on the native data used in the final refinements are in Table 1.

The details of the data collection and refinement are in the Supplemental Experimental Procedures. All of the structure figures were made with CCP4MG (Potterton et al., 2002).

Circular Dichroism Spectroscopy

Concentrated proteins were diluted to 10 μM in 50 mM $NaPO_4$ (pH 8.0) for analysis on a Jasco J-815 CD spectrometer. Far UV CD spectra (190–240 nm) were measured at 20°C with a 20 nm/min scan rate in a 0.1 cm path-length cuvette. The thermal denaturation measurements were performed at 0.5°C/min from 20°C to 70°C while monitoring the CD signal at 225 nm. The data were fit by non-linear regression with Grace (http://plasma-gate.weizmann.ac.il/Grace/) to a two-state transition with the equation

$$y_{obs} = \frac{(m_n T + b_n) + (m_d T + b_d)\{\exp[\Delta H_m / R \cdot (1/T_m - 1/T)]\}}{\{1 + \exp[\Delta H_m / R \cdot (1/T_m - 1/T)]\}}$$

in which y_{obs} is the CD signal at 225 nm, T is the temperature in Kelvin, R is the gas constant, T_m is the midpoint of the unfolding transition in Kelvin, and ΔH_m is the enthalpy of unfolding at this temperature (Swint and Robertson, 1993). The m and b terms with the n and d subscripts are the slopes and y intercepts of the baselines for the native and denatured states, respectively.

The NMR data collection, chemical shift assignment, and PFD aggregation kinetics are described in the Supplemental Experimental Procedures.

Aggregation Prediction Algorithms

We chose three aggregation prediction algorithms that use different prediction methods and applied them to the sequences of HET-s and HET-S. Significant score levels were determined according to the authors' recommendations, and the consensus regions were mapped to the structure of HET-S and visualized with CCP4MG. The three programs used were TANGO (Fernandez-Escamilla et al., 2004), PASTA (Trovato et al., 2007), and SALSA (Zibaee et al., 2007).

HET-S$^{(1-227)(218-289)}$ and PFD Mutant Analysis

All site-directed *het-S* mutants were generated using the QuikChange Site-Directed Mutagenesis kit (Stratagene). Mutations were introduced into pCB1004-*het-S* or pGPD-*het-S*-GFP (Coustou-Linares et al., 2001). The details of the HET-S$^{(1-227)(218-289)}$ construction and design are in the Supplemental Experimental Procedures. The properties of the *het-S* mutant alleles were determined by transforming the mutated plasmid bearing the *hyg^R* marker into a *Δhet-s* strain (Turcq et al., 1991). Transformants were selected and each transformant was confronted on solid medium with a wild-type [Het-s] strain in barrage tests.

In Vivo Localization of HET-s and HET-S

A *Δhet-s* strain was cotransformed with the pGPD-*het-S*-GFP (Coustou-Linares et al., 2001) and pGPD-*het-s*-RFP plasmids. Transformants were selected and analyzed by fluorescence microscopy. For fluorescence microscopy, synthetic medium containing 2% (wt/vol) agarose was used. *P. anserina* hyphae were inoculated on this medium and cultivated for 16–24 hr at 26°C. The mycelium was examined in situ with a Leica DMRXA microscope equipped with a Micromax CCD (Princeton Instruments) controlled by the Metamorph 5.06 software (Roper Scientific). The microscope was fitted with a standard FITC filter set (Leica L4) and a Leica PL APO 100× immersion objective.

ACCESSION NUMBERS

Structure factors and coordinates were deposited in the Protein Data Bank (see Table 1).

SUPPLEMENTAL INFORMATION

Supplemental Information includes Supplemental Experimental Procedures, eight figures, three tables, and Supplemental References and can be found with this article at doi:10.1016/j.molcel.2010.05.019.

ACKNOWLEDGMENTS

This work was supported by grants from the Schweizerische Nationalfonds (SNF) and the National Institutes of Health (NIH). S.J.S. was supported by an Agence Nationale de la Recherche (ANR) grant "PANPRIONDRUG." Portions of this research were carried out at Stanford Synchrotron Radiation Lightsource (SSRL), supported by the Department of Energy (DOE), Office of Biological and Environmental Research, the NIH, National Center for Research Resources, Biomedical Technology Program, and the National Institute of

General Medical Sciences. The Advanced Light Source (ALS) is supported by the DOE, Office of Basic Energy Sciences, under Contract No. DE-AC02-05CH11231. The expertise of Alexander Sobol was of valuable assistance and is gratefully acknowledged.

Received: November 26, 2009
Revised: February 26, 2010
Accepted: April 15, 2010
Published: June 24, 2010

REFERENCES

Aguzzi, A., Sigurdson, C., and Heikenwaelder, M. (2008). Molecular mechanisms of prion pathogenesis. Annu. Rev. Pathol. *3*, 11–40.

Balguerie, A., Dos Reis, S., Ritter, C., Chaignepain, S., Coulary-Salin, B., Forge, V., Bathany, K., Lascu, I., Schmitter, J.M., Riek, R., and Saupe, S.J. (2003). Domain organization and structure-function relationship of the HET-s prion protein of *Podospora anserina*. EMBO J. *22*, 2071–2081.

Balguerie, A., Dos Reis, S., Coulary-Salin, B., Chaignepain, S., Sabourin, M., Schmitter, J.M., and Saupe, S.J. (2004). The sequences appended to the amyloid core region of the HET-s prion protein determine higher-order aggregate organization in vivo. J. Cell Sci. *117*, 2599–2610.

Beisson-Schecroun, J. (1962). Incompatibilité cellulaire et interactions nucléo-cytoplamsiques dans les phénomènes de barrage chez le *Podospora anserina*. Ann. Genet. *4*, 3–50.

Coustou, V., Deleu, C., Saupe, S., and Begueret, J. (1997). The protein product of the het-s heterokaryon incompatibility gene of the fungus *Podospora anserina* behaves as a prion analog. Proc. Natl. Acad. Sci. USA *94*, 9773–9778.

Coustou, V., Deleu, C., Saupe, S.J., and Begueret, J. (1999). Mutational analysis of the [Het-s] prion analog of *Podospora anserina*. A short N-terminal peptide allows prion propagation. Genetics *153*, 1629–1640.

Coustou-Linares, V., Maddelein, M.L., Begueret, J., and Saupe, S.J. (2001). In vivo aggregation of the HET-s prion protein of the fungus *Podospora anserina*. Mol. Microbiol. *42*, 1325–1335.

Dalstra, H.J., Swart, K., Debets, A.J., Saupe, S.J., and Hoekstra, R.F. (2003). Sexual transmission of the [Het-S] prion leads to meiotic drive in *Podospora anserina*. Proc. Natl. Acad. Sci. USA *100*, 6616–6621.

Dehay, B., and Bertolotti, A. (2006). Critical role of the proline-rich region in Huntingtin for aggregation and cytotoxicity in yeast. J. Biol. Chem. *281*, 35608–35615.

de la Fortelle, E., and Bricogne, G. (1997). Maximum-Likelihood Heavy-Atom Parameter Refinement for the Multiple Isomorphous Replacement and Multiwavelength Anomalous Diffraction Methods, *Volume 276* (New York: Academic Press).

Deleu, C., Clave, C., and Begueret, J. (1993). A single amino acid difference is sufficient to elicit vegetative incompatibility in the fungus *Podospora anserina*. Genetics *135*, 45–52.

Diederichs, K., and Karplus, P.A. (1997). Improved R-factors for diffraction data analysis in macromolecular crystallography. Nat. Struct. Biol. *4*, 269–275.

Duennwald, M.L., Jagadish, S., Muchowski, P.J., and Lindquist, S. (2006). Flanking sequences profoundly alter polyglutamine toxicity in yeast. Proc. Natl. Acad. Sci. USA *103*, 11045–11050.

Engh, R.A., and Huber, R. (1991). Accurate bond and angle parameters for X-ray protein structure refinement. Acta Crystallogr. A *47*, 392–400.

Fernandez-Bellot, E., Guillemet, E., and Cullin, C. (2000). The yeast prion [URE3] can be greatly induced by a functional mutated URE2 allele. EMBO J. *19*, 3215–3222.

Fernandez-Escamilla, A.M., Rousseau, F., Schymkowitz, J., and Serrano, L. (2004). Prediction of sequence-dependent and mutational effects on the aggregation of peptides and proteins. Nat. Biotechnol. *22*, 1302–1306.

Glabe, C.G. (2006). Common mechanisms of amyloid oligomer pathogenesis in degenerative disease. Neurobiol. Aging *27*, 570–575.

Glass, N.L., Jacobson, D.J., and Shiu, P.K. (2000). The genetics of hyphal fusion and vegetative incompatibility in filamentous ascomycete fungi. Annu. Rev. Genet. *34*, 165–186.

Kay, L.E., Torchia, D.A., and Bax, A. (1989). Backbone dynamics of proteins as studied by 15N inverse detected heteronuclear NMR spectroscopy: application to staphylococcal nuclease. Biochemistry *28*, 8972–8979.

Krissinel, E., and Henrick, K. (2007). Inference of macromolecular assemblies from crystalline state. J. Mol. Biol. *372*, 774–797.

Liu, J.J., Sondheimer, N., and Lindquist, S.L. (2002). Changes in the middle region of Sup35 profoundly alter the nature of epigenetic inheritance for the yeast prion. Proc. Natl. Acad. Sci. USA *99* (*Suppl 4*), 16446–16453.

Maddelein, M.L., and Wickner, R.B. (1999). Two prion-inducing regions of Ure2p are nonoverlapping. Mol. Cell. Biol. *19*, 4516–4524.

Masison, D.C., and Wickner, R.B. (1995). Prion-inducing domain of yeast Ure2p and protease resistance of Ure2p in prion-containing cells. Science *270*, 93–95.

Mayer, M., and Meyer, B. (2001). Group epitope mapping by saturation transfer difference NMR to identify segments of a ligand in direct contact with a protein receptor. J. Am. Chem. Soc. *123*, 6108–6117.

Paoletti, M., and Clave, C. (2007). The fungus-specific HET domain mediates programmed cell death in *Podospora anserina*. Eukaryot. Cell *6*, 2001–2008.

Potterton, E., McNicholas, S., Krissinel, E., Cowtan, K., and Noble, M. (2002). The CCP4 molecular-graphics project. Acta Crystallogr. D Biol. Crystallogr. *58*, 1955–1957.

Ritter, C., Maddelein, M.L., Siemer, A.B., Luhrs, T., Ernst, M., Meier, B.H., Saupe, S.J., and Riek, R. (2005). Correlation of structural elements and infectivity of the HET-s prion. Nature *435*, 844–848.

Rizet, G. (1952). Les phénomènes de barrage chez *Podospora anserina*. I. Analyse de barrage entre les souches s et S. Rev. Cytol. Biol. Veg. *13*, 51–92.

Sabate, R., Castillo, V., Espargaro, A., Saupe, S.J., and Ventura, S. (2009). Energy barriers for HET-s prion forming domain amyloid formation. FEBS J. *276*, 5053–5064.

Saupe, S.J. (2000). Molecular genetics of heterokaryon incompatibility in filamentous ascomycetes. Microbiol. Mol. Biol. Rev. *64*, 489–502.

Swint, L., and Robertson, A.D. (1993). Thermodynamics of unfolding for turkey ovomucoid third domain: thermal and chemical denaturation. Protein Sci. *2*, 2037–2049.

Trovato, A., Seno, F., and Tosatto, S.C. (2007). The PASTA server for protein aggregation prediction. Protein Eng. Des. Sel. *20*, 521–523.

Turcq, B., Deleu, C., Denayrolles, M., and Begueret, J. (1991). Two allelic genes responsible for vegetative incompatibility in the fungus *Podospora anserina* are not essential for cell viability. Mol. Gen. Genet. *228*, 265–269.

Wasmer, C., Lange, A., Van Melckebeke, H., Siemer, A.B., Riek, R., and Meier, B.H. (2008). Amyloid fibrils of the HET-s(218-289) prion form a beta solenoid with a triangular hydrophobic core. Science *319*, 1523–1526.

Wasmer, C., Schutz, A., Loquet, A., Buhtz, C., Greenwald, J., Riek, R., Bockmann, A., and Meier, B.H. (2009). The molecular organization of the fungal prion HET-s in its amyloid form. J. Mol. Biol. *394*, 119–127.

Wickner, R.B., Shewmaker, F., Kryndushkin, D., and Edskes, H.K. (2008). Protein inheritance (prions) based on parallel in-register beta-sheet amyloid structures. Bioessays *30*, 955–964.

Zibaee, S., Makin, O.S., Goedert, M., and Serpell, L.C. (2007). A simple algorithm locates beta-strands in the amyloid fibril core of alpha-synuclein, Abeta, and tau using the amino acid sequence alone. Protein Sci. *16*, 906–918.